SAMPLE

12

14 — CPU

20 — FOURIER PROCESSOR

22 — COMBINATION PROCESSOR

24 — RECONSTRUCT PROCESSOR

26 — SPATIAL FILTER

28 — SHIFT VARIANT FILTER

30 — SQUARED TRIG FUNCTION

32 — ARITHMETIC PROCESSOR

28 — DISPLAY

16 — MENU SELECT

10

FIG. 1

100 COLLECT SAMPLES

102 FAST FOURIER TRANSFORM SAMPLES

104 FORM LINEAR COMBINATION OF COMPLEMENTARY DATA ELEMENTS

106 FILTER COMBINATION IN SPATIAL DOMAIN

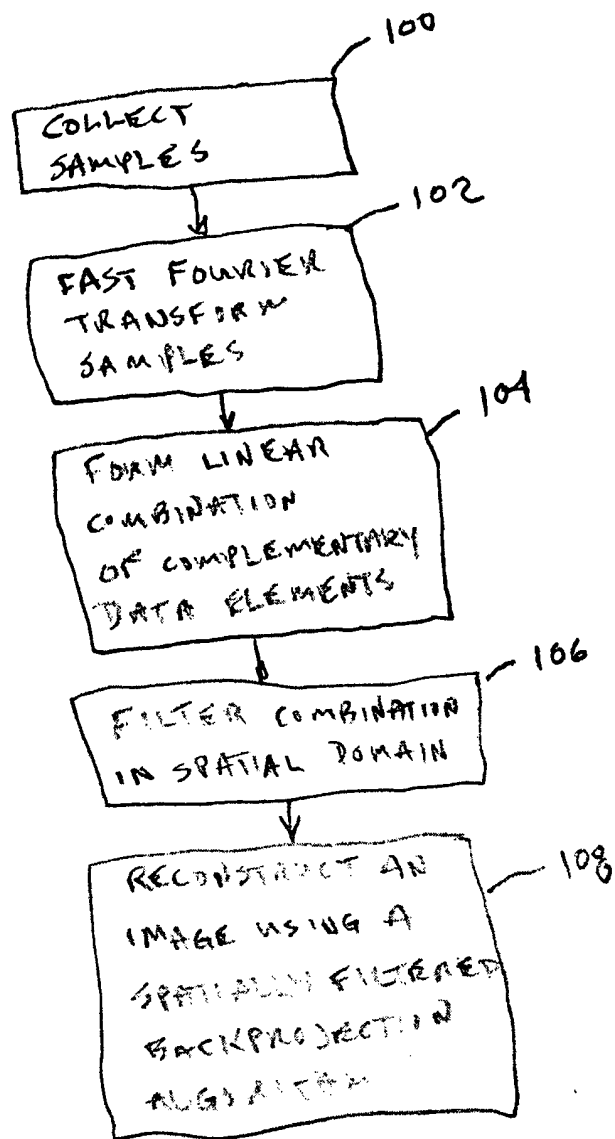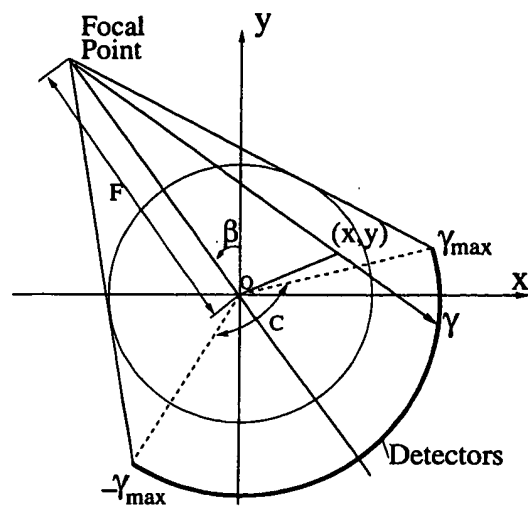108 RECONSTRUCT AN IMAGE USING A SPATIALLY FILTERED BACKPROJECTION ALGORITHM

FIG. 2

Figure 3   The fan-beam geometry in CT, where $2\gamma_{max}$ denotes the maximum fan angle of the curved detector array with respect to the focal source, the focal length F is the distance between the focal source and the center of rotation, and the center fan angle C denotes the maximum fan angle of the curved detector array with respect to the center of rotation.
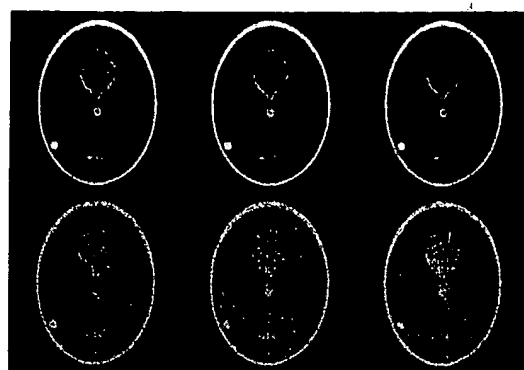
(a)
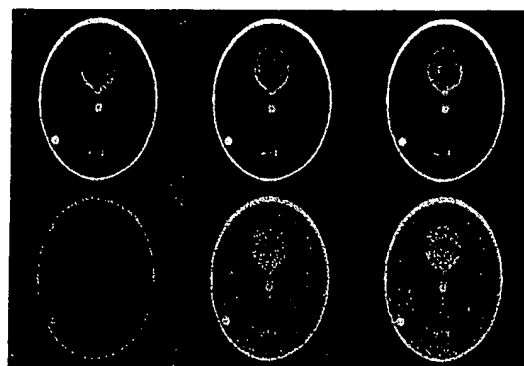
(b)

Figure 4 Images reconstructed from fan-beam sinograms generated with configurations (a) and (b), respectively. Images in the first and second rows were reconstructed from noiseless and noisy fan-beam sinograms by use of the FFBP (1st column), the new hybrid (2nd column), and the previous hybrid (3rd column) algorithms.
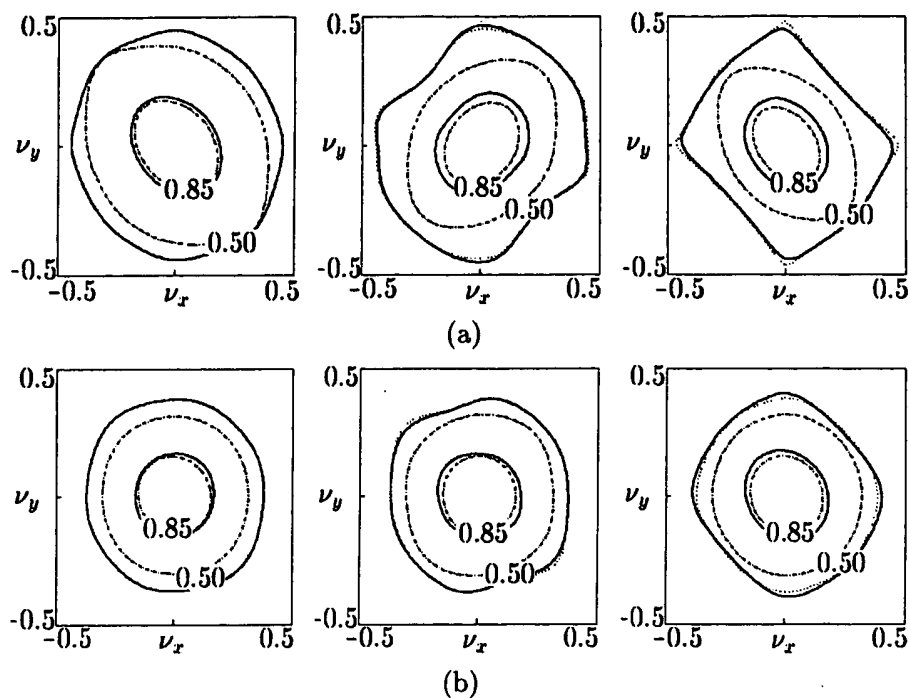
Figure 5 Contours of the moduli of the Fourier transforms (normalized to their maxima) of recon-structed images containing points on pixels (68, 68) (1st column), (80, 48) (2nd column), and (90, 90) (the 3rd column) for configurations (a) (1st row) and (b) (2nd row), respectively. The dotted, solid, and dash-dotted curves denote the results obtained with the FFBP, the new hybrid, and the previous hybrid algorithms, respectively.
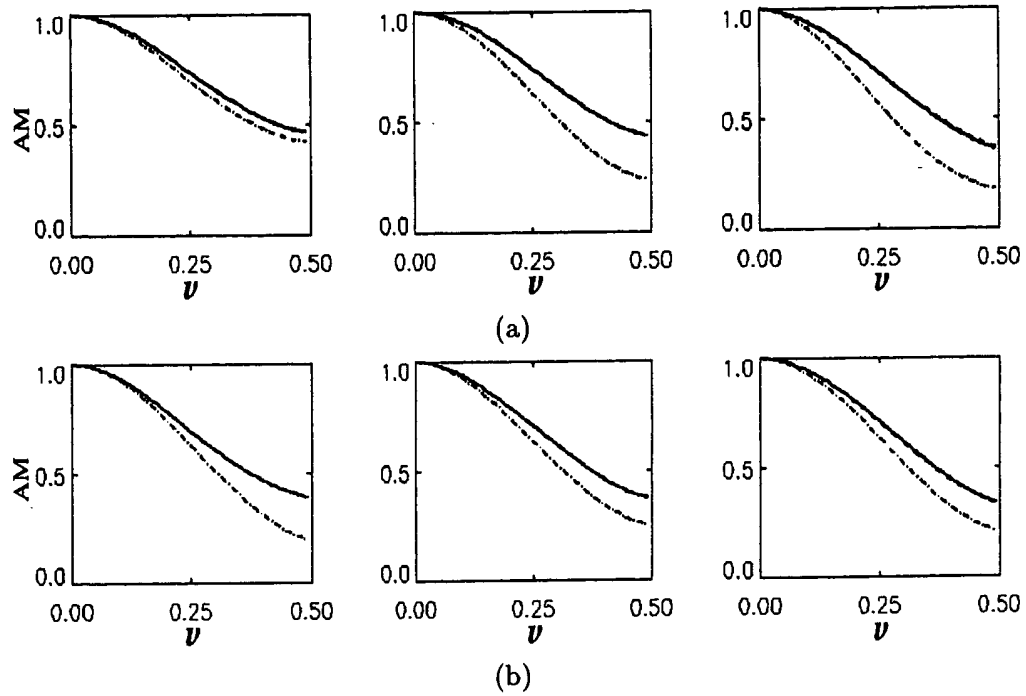
Figure 6 Average moduli (AMs) of the Fourier transforms (normalized to their maxima) of reconstructed images containing points on pixels (68, 68) (1st column), (80, 48) (2nd column), and (90, 90) (3rd column) for configurations (a) (1st row) and (b) (2nd row), respectively. The dotted, solid, and dash-dotted curves denote AMs obtained with the FFBP, the new hybrid, and the previous hybrid algorithms, respectively.
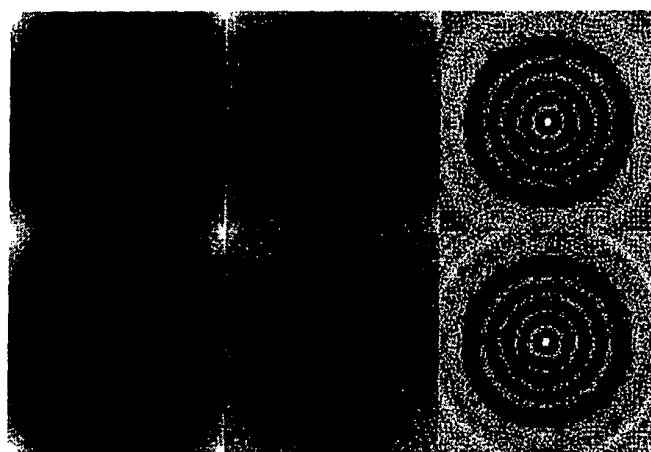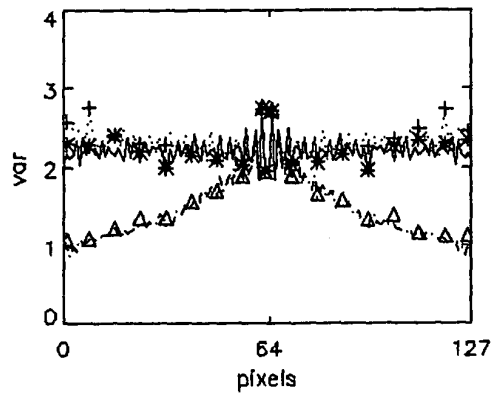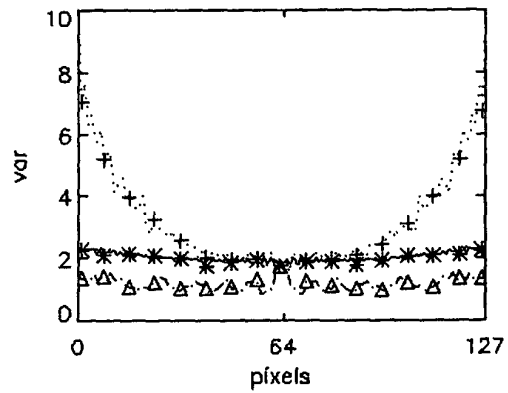
Figure 7 Variance-images obtained with the FFBP (1st column), the new hybrid (2nd column), and the previous hybrid (3rd column) algorithms for configuration (a) and (b). The theoretical and empirical results are shown in the first and second rows, respectively.

(a)

(b)

Figure 8 Theoretical profiles on the center rows in variance-images obtained with the FFBP (the dotted curve), the new hybrid (the solid curve), and the previous hybrid (the dash-dotted curve) algorithms for configurations (a) and (b). Empirical results obtained with the FFBP (+), the new hybrid (*), and the previous hybrid (Δ) algorithms are also displayed.
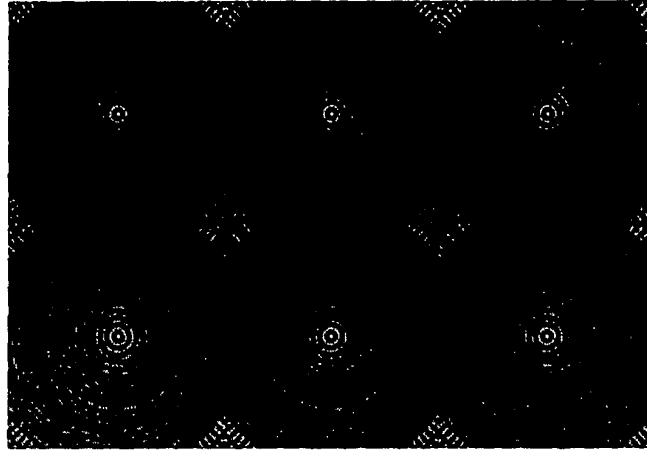
Figure 9 Variance-images obtained for a fan-beam configuration with a focal length $F = 50000$ pixels by use of the FFBP (1st column), the new hybrid (2nd column), and the previous hybrid (3rd column). The theoretical and empirical results are displayed in the first and second rows, respectively.
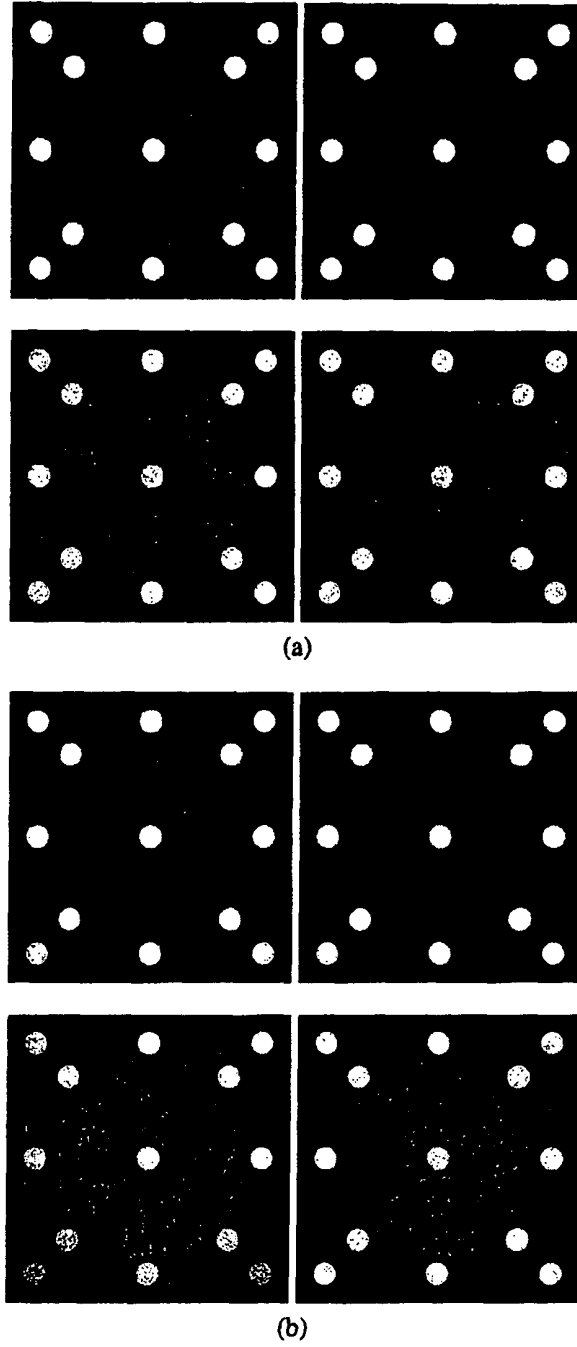
Figure 10 Images of the bead phantom reconstructed by use of the half-scan FFBP algorithm (left column) and the proposed algorithm (right column) from noiseless (upper row) and noisy (lower row) half-scan data generated with fan-beam configuration (a): $F = 850$ mm, $\gamma_{max} = 0.09\pi$ and configuration (b): $F = 250$ mm, $\gamma_{max} = 0.34\pi$, respectively. A display window [-1000HU, 1000HU] was used.
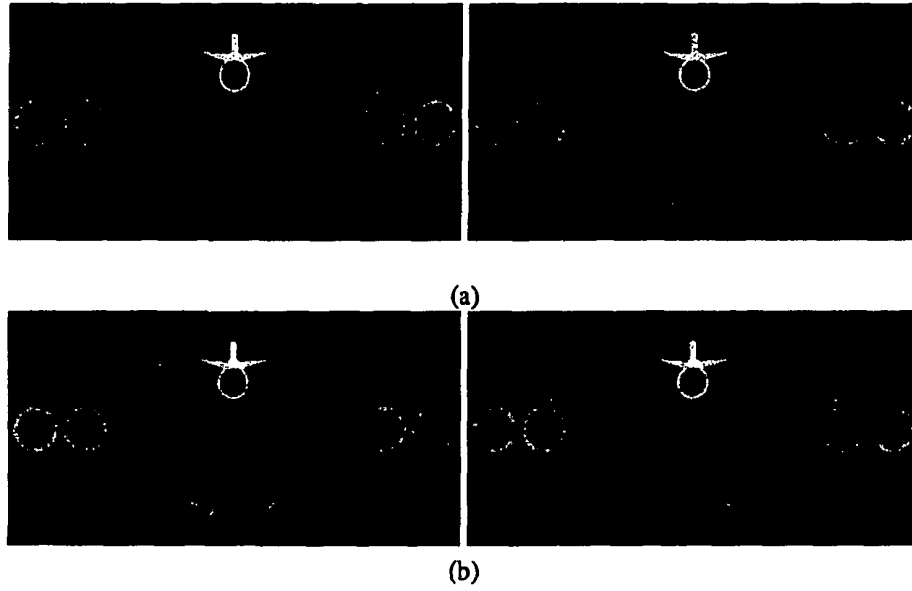
16

(a)

(b)

Figure 1: Images of the Thorax/Shoulder phantom reconstructed by use of the half-scan FFBP algorithm (left column) and the proposed half-scan algorithm (right column) from noisy half-scan data generated with fan-beam configuration (a): $F = 850$ mm, $\gamma_{max} = 0.09\pi$ and configuration (b): $F = 250$ mm, $\gamma_{max} = 0.34\pi$, respectively. A display window [-1000HU, 1000HU] was used.
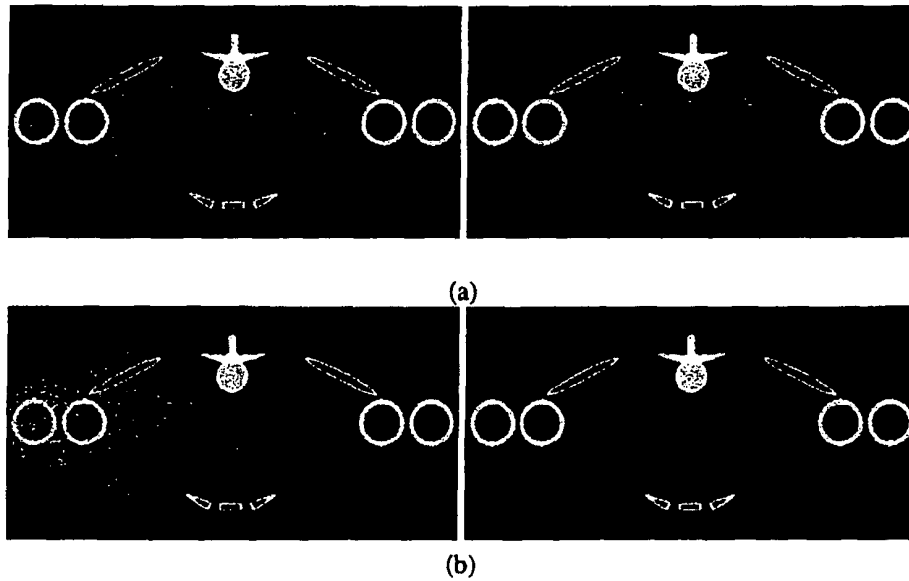

(a)

(b)

Figure 2: Same images as those in Fig. 3, but displayed with a grayscale window [-100HU, 200HU].
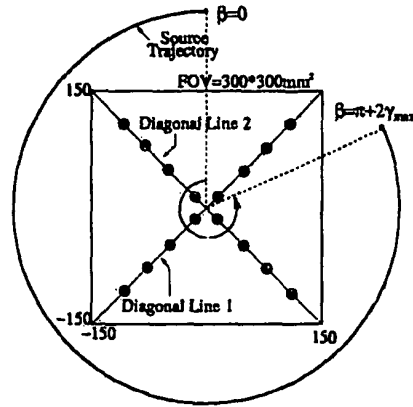
17

Figure ⟨3 Locations at which the resolution properties of the two algorithms are evaluated.
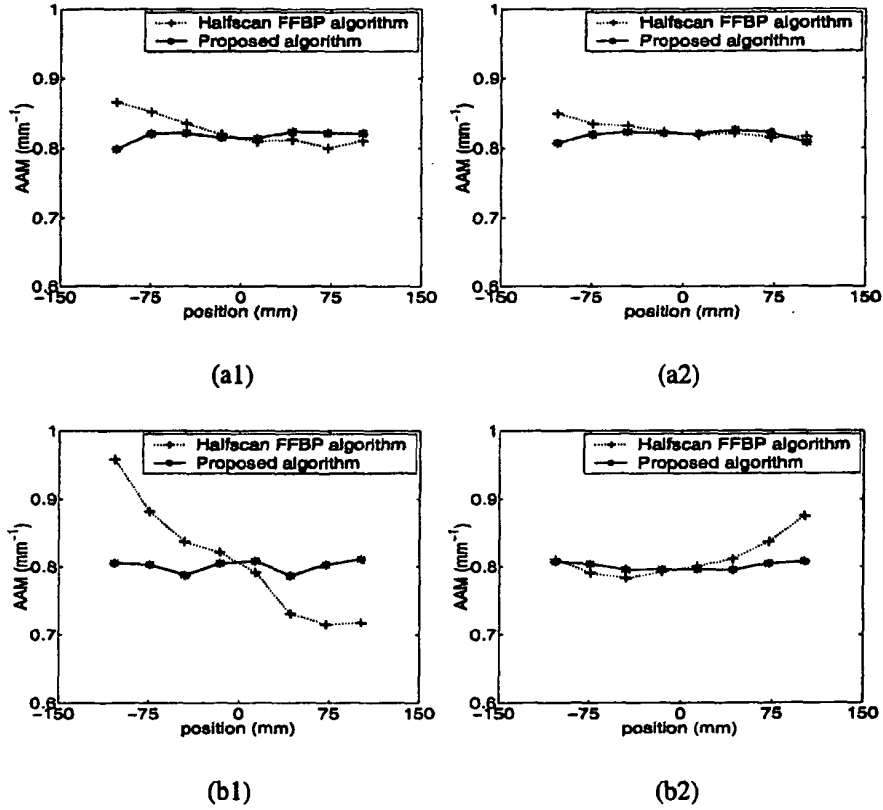

(a1)

(a2)

(b1)

(b2)

Figure ⟨4: Panels (a1), (a2) and panels (b1), (b2) display the AAMs on diagonal lines 1 and 2, as shown in Fig. 5, obtained for configurations (a) and (b), respectively. It can be seen that the AAMs of the proposed half-scan algorithm are much more uniform than those of the half-scan FFBP algorithm.
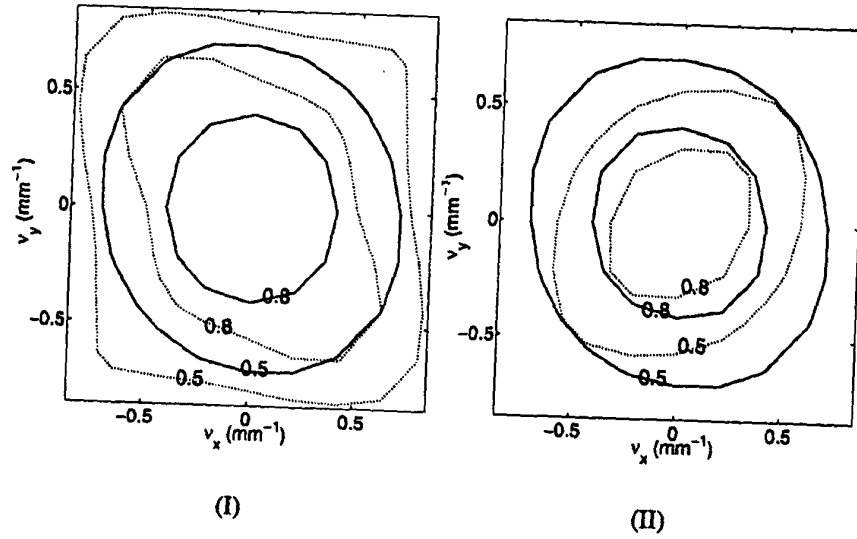
18

(I)   (II)

Figure 15: Contour plots of the Fourier transform moduli of the reconstructed point-like structures at (I) (-102mm, -102mm) and (II) (102mm, 102mm) for fan-beam configuration (b) obtained with the half-scan FFBP algorithm (dotted curves) and the proposed half-scan algorithm (solid curves). The highly non-circular contour shapes obtained with the half-scan FFBP algorithm indicate that the half-scan FFBP algorithm yields images with more significant distortions than does the proposed algorithm.

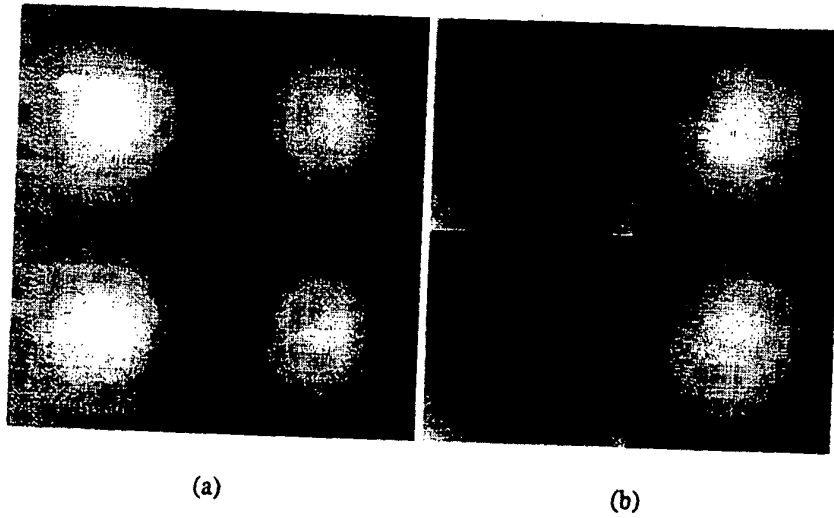
(a)   (b)

Figure 16: Image-variances obtained with the half-scan FFBP algorithm(left column) and the proposed half-scan algorithm (right column) for configuration (a) and (b), respectively. The theoretical and empirical results are shown in the top and bottom rows, respectively.
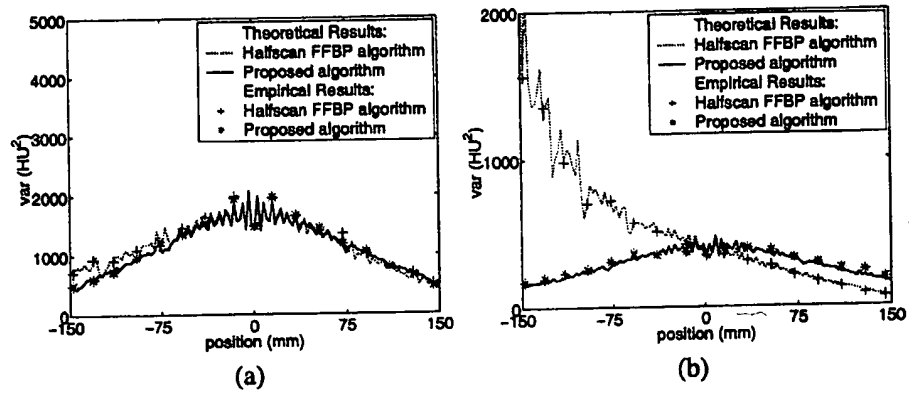
19

(a)

(b)

Figure 17 Theoretical profiles along the central-horizontal rows in image-variances obtained with the half-scan FFBP algorithm (the dotted curve) and the proposed half-scan algorithm (the solid curve) for configurations (a) and (b), respectively. Empirical results obtained with the half-scan FFBP algorithm (+) and the proposed half-scan algorithm (*) are also displayed.
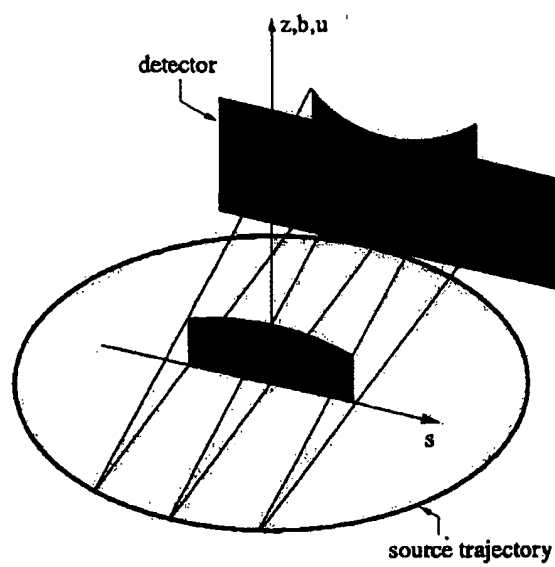
Figure 18. Vertically-parallel fan-beam data that are obtained by rebinning the cone-beam data acquired with a circular orbit.
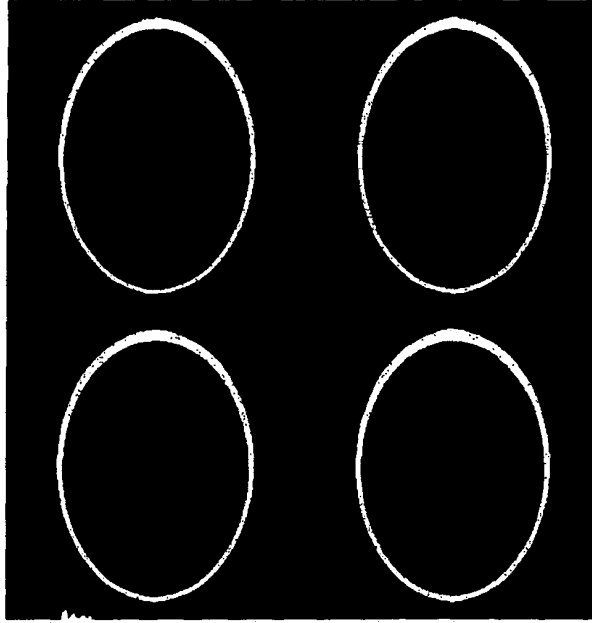
Figure 19 Images for a slice at $y = -37.5$ mm in the Shepp-Logan phantom by use of the FDK algorithm (upper left), the T-FDK algorithm (upper right), the proposed algorithm (lower left), and the proposed algorithm without cone-angle weighting (lower right), respectively. All images are showed in a gray-scale window [0, 60HU].
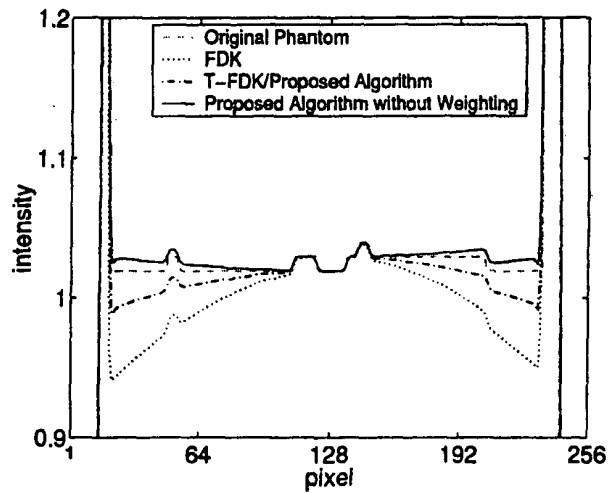

Figure 20 Profiles along an axis parallel to the z-axis with $x = 0$ mm, $y = -37.5$ mm in the reconstructed 3D Shepp-Logan images by use of the FDK algorithm (dotted), the T-FDK algorithm (dash-dotted), the proposed algorithm (overlapping with that of the T-FDK algorithm), and the proposed algorithm without cone-angle weighting (solid). The profile of the original phantom at the same position is drawn in dashed curve.
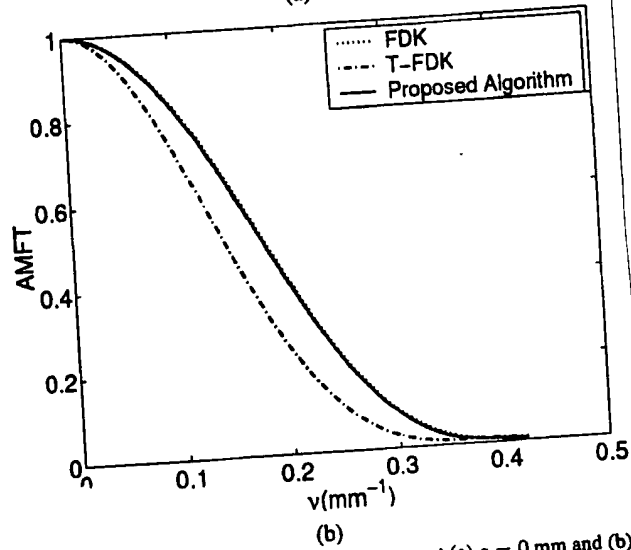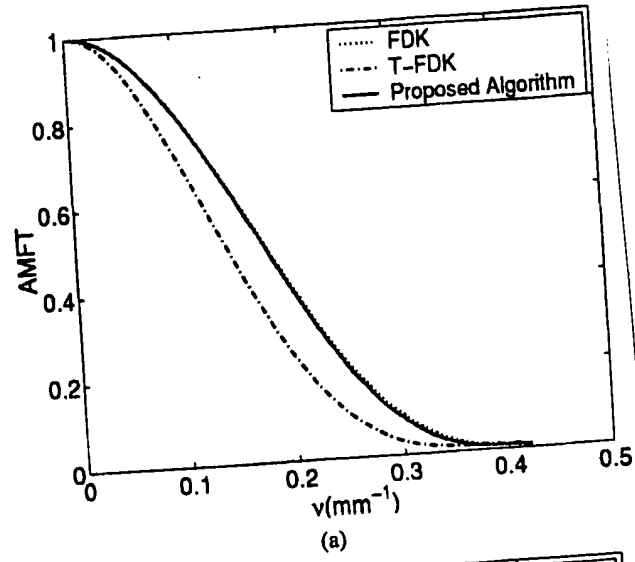
(a)

(b)

Figure 21: The AMFTs obtained for 2D images at (a) $z = 0$ mm and (b) $z = 37.5$ mm. The dotted, dashed, and the solid curves were obtained by use of the FDK algorithm, the T-FDK algorithm, and the proposed algorithm, respectively.
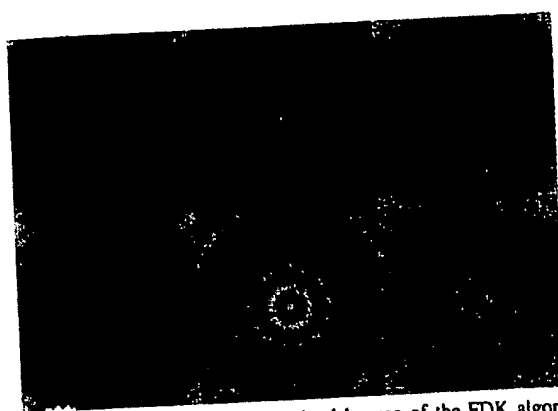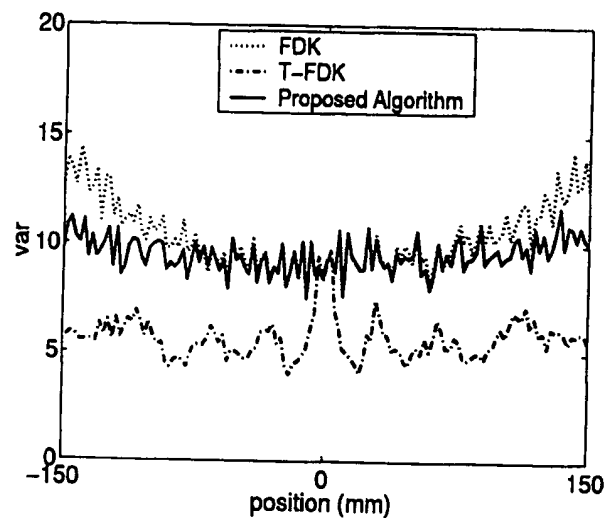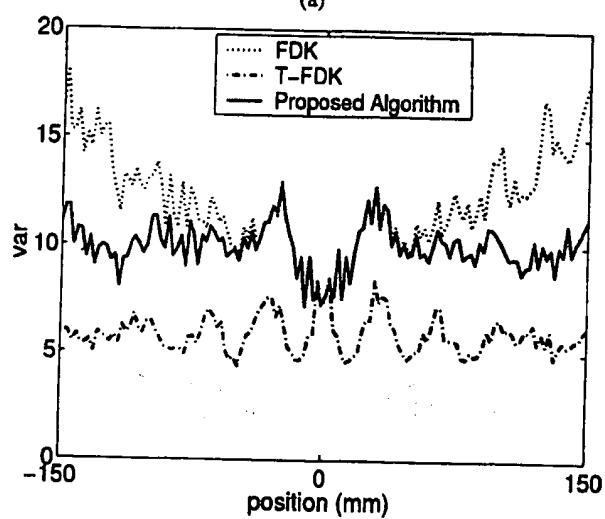
Figure 22: 2D variance-images obtained by use of the FDK algorithm (left column), the T-FDK algorithm (middle column), and the proposed algorithm (right column) at $z = 0$ mm (first row) and $z = 37.5$ mm (second row), respectively.
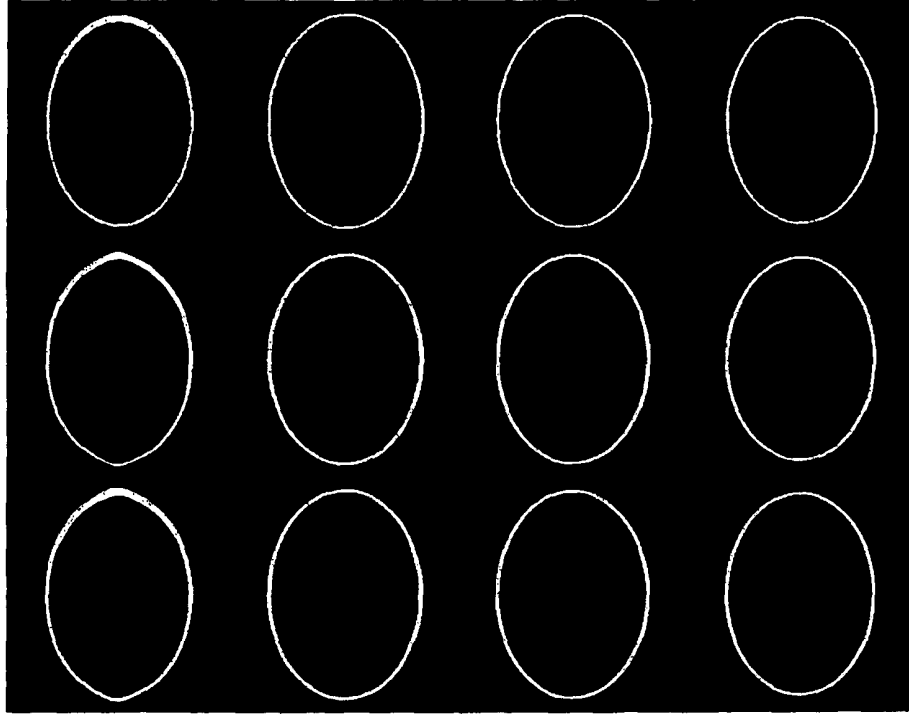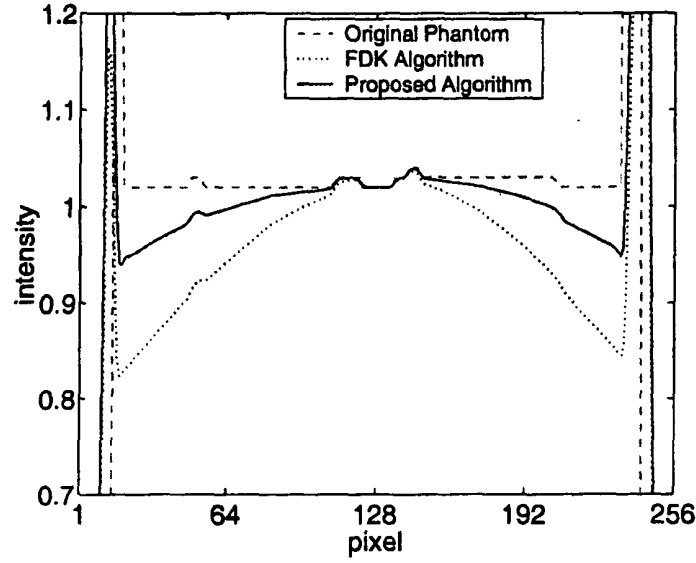
(a)

(b)

Figure 23 Profiles along the center columns in 2D variance-images in
Fig22 at (a) $z = 0$ mm and (b) $z = 37.5$ mm, respectively. The dotted
curve, the dashed curve, and the solid curve were obtained by use of
the FDK algorithm, the T-FDK algorithm, and the proposed algorithm,
respectively.

Figure 24 Asymmetric cone-beam CT configuration.

(a)

(b)

Figure 25 (a) Images for slices at $y = -37.5$ mm (first column), $z = 0$ mm (second column), $z = 18.8$ mm (third column), and $z = 37.5$ mm (forth column) in the 3D Shepp-Logan phantom. The first, second, and third rows show the corresponding slices in the original phantom, the images reconstructed by the FDK algorithm, the images reconstructed by the proposed algorithm, respectively. (b) Profiles along the center column (z direction) of the images in first column of (a).

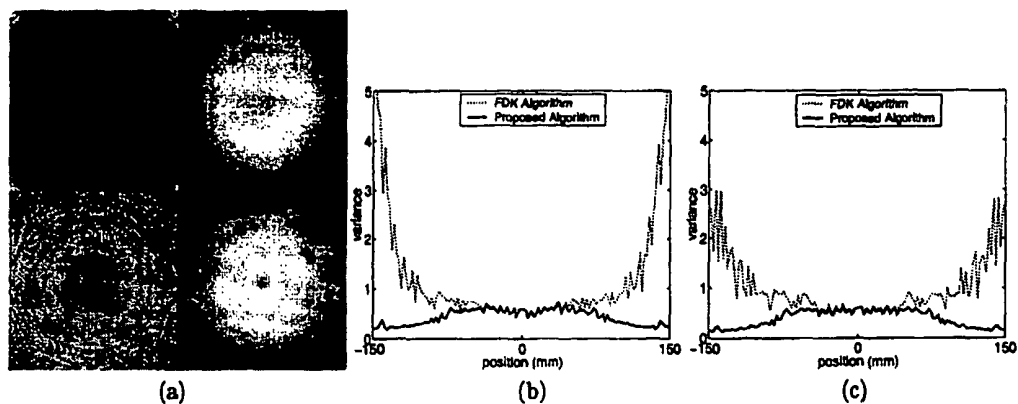(a)   (b)   (c)

Figure 26 (a) 2D variance-images at $z = 0$ mm (upper row) and $z = 37.5$ mm (lower row) obtained by use of the FDK algorithm (left column) and the proposed algorithm (right column). (b-c)Profiles along the diagonal lines of the variance-images in the first and second rows of (a).
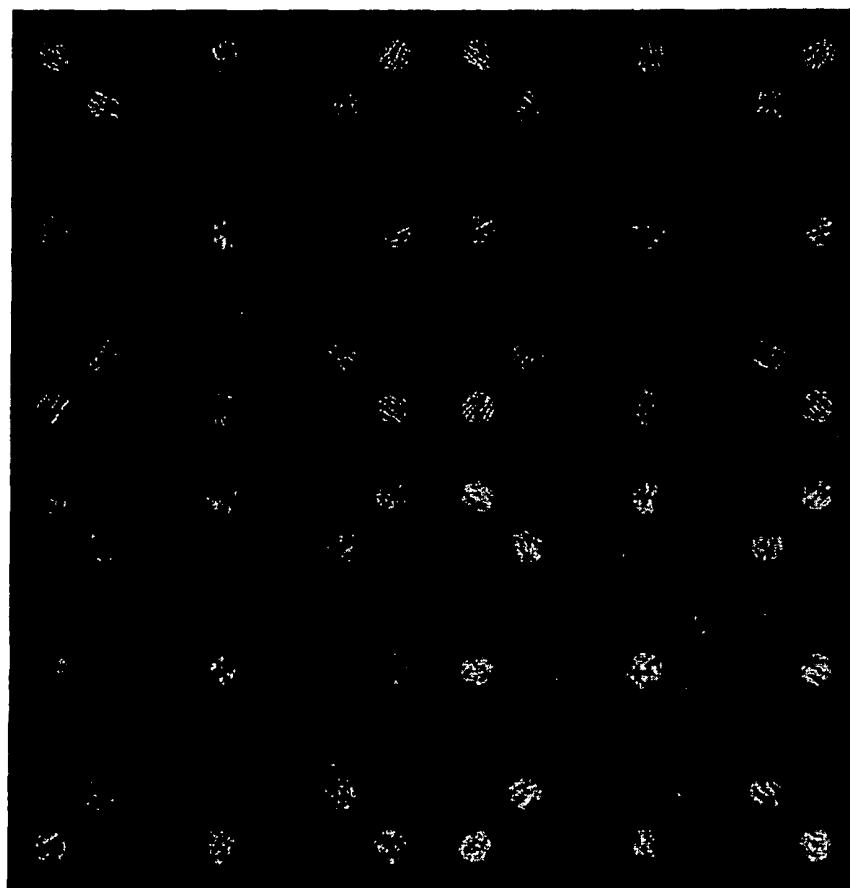

Figure 27 Reconstructed images by use of the FDK algorithm (upper row) and the proposed algorithm (lower row) for 2D slices at $z = 0$ mm (left column) and $z = 37.5$ mm (right column) from noisy data generated with the asymmetric cone-beam configurations.
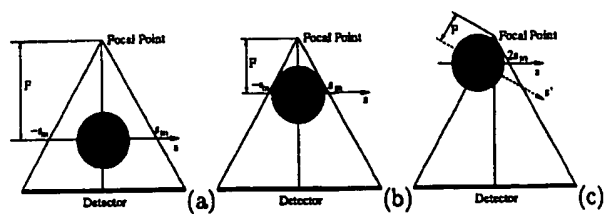
4

Fig.28 Fan-beam configuration with a fixed maximum fan-angle that is
determined by the size of the detector and its distance to the focal spot.
(a) and (b) show configurations in which the center of a given FOV (i.e,
the object) is placed at different distances from the focal spot. (c) displays
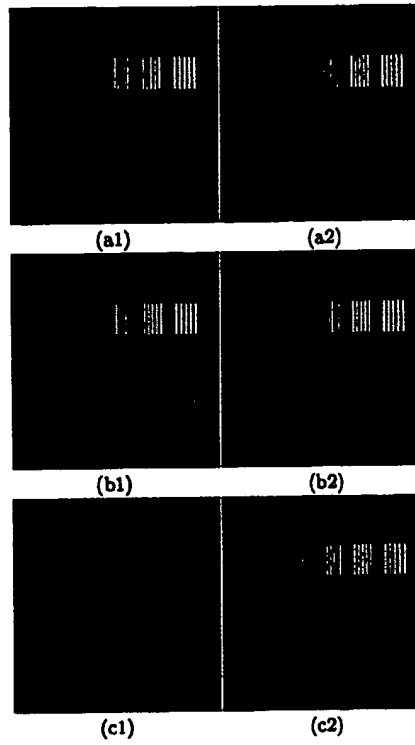the asymmetric scanning configuration.

(a1)   (a2)

(b1)   (b2)

(c1)   (c2)

Fig. 29. Images reconstructed with the FFBP algorithm (1) and the proposed algorithm (2) for the three configurations (a), (b), and (c) shown in Fig. 1.
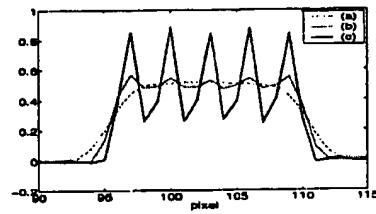

Fig 30. Profiles of the finest bar pattern in Fig. 2(a2), (b2), and (c2).